Journal Pre-proof

High-performance Flexible Hybrid Supercapacitor Based on NiAl Layered Double Hydroxide as a Positive Electrode and Nitrogen-Doped Reduced Graphene Oxide as a Negative electrode

Min Li, Mathias Dolci, Pascal Roussel, Alexandre Barras, Sabine Szunerits, Rabah Boukherroub

PII: S0013-4686(20)31057-4

DOI: https://doi.org/10.1016/j.electacta.2020.136664

Reference: EA 136664

To appear in: *Electrochimica Acta*

Received Date: 8 May 2020

Revised Date: 16 June 2020

Accepted Date: 21 June 2020

Please cite this article as: M. Li, M. Dolci, P. Roussel, A. Barras, S. Szunerits, R. Boukherroub, High-performance Flexible Hybrid Supercapacitor Based on NiAl Layered Double Hydroxide as a Positive Electrode and Nitrogen-Doped Reduced Graphene Oxide as a Negative electrode, *Electrochimica Acta*, https://doi.org/10.1016/j.electacta.2020.136664.

Credit Author Statement

Min Li: Conceptualization, Investigation

Mathias Dolci: Investigation

Pascal Roussel: Investigation

Alexandre Barras: Investigation

Sabine Szunerits: Investigation, Writing - Review & Editing

Rabah Boukherroub: Conceptualization, Supervision, Project administration, Writing - Review & Editing, Funding acquisition

High-performance Flexible Hybrid Supercapacitor Based on NiAl Layered Double Hydroxide as a Positive Electrode and Nitrogen-Doped Reduced Graphene Oxide as a Negative electrode

Min Li,[1] Mathias Dolci,[1] Pascal Roussel,[2] Alexandre Barras[1], Sabine Szunerits[1] and Rabah Boukherroub[1*]

[1]*Univ. Lille, CNRS, Centrale Lille, Univ. Polytechnique Hauts-de-France, UMR 8520 - IEMN, F-59000 Lille, France*

[2]*Univ. Lille, CNRS, ENSCL, Centrale Lille, Univ. Artois, UMR8181, UCCS-Unité de Catalyse et Chimie du Solide, Lille, F-59000, France*

*To whom correspondence should be addressed: Rabah Boukherroub (rabah.boukherroub@univ-lille.fr; Tel: +33 3 62 53 17 24)

Abstract

Herein, we investigated the influence of Fe, Cr and Al incorporation in Ni-based layered double hydroxides (LDHs) supported on nickel foam (NF) electrodes, prepared through a one-step hydrothermal, on their electrochemical performance. The resulting NiFe, NiCr and NiAl (LDHs) were further coated on carbon spheres (CS) supported on NF using a facile two-step hydrothermal process to produce NiFe LDHs@CS/NF, NiCr LDHs@CS/NF and NiAl LDHs@CS/NF. The performance of the prepared materials as binder-free electrodes in supercapacitors was assessed. Among all the prepared electrodes, NiAl LDHs@CS/NF electrode material achieved the largest areal capacity (1042.2 mC cm^{-2} at 1 mA cm^{-2}), as compared to the areal capacity values attained by NiFe LDHs@CS/NF (705.8 mC cm^{-2}) and NiCr LDHs@CS/NF (814.9 mC cm^{-2}) at 1 mA cm^{-2}. Therefore, a hybrid supercapacitor device comprising NiAl LDHs@CS/NF as the positive electrode and N-doped reduced graphene/NF as the negative electrode was successfully fabricated. The device exhibited favorable flexibility, good mechanical properties and stability (the areal capacity remained ~75% and ~67% of the original value after 5,000 and 10,000 cycles, respectively). The hybrid supercapacitor attained an energy density of 43 μWh cm^{-2} at a power density of 0.805 mW cm^{-2} and was applied successfully to operate a home-made windmill device continuously for 32 s. Moreover, two flexible NiAl LDHs@CS/NF//N-rGO/NF hybrid supercapacitors, connected in series, were able to light up a green, a red and a yellow LED in parallel, lasting for 37 s, 542 s and 199 s, respectively, indicating their potential application for flexible energy storage devices.

Keywords: *NiAl LDHs, Carbon spheres, Nickel foam; Flexible Supercapacitors.*

1. Introduction

In the last few years, wearable electronic devices attracted widespread attention, and consequently led to a steady increase demand of energy storage devices with enhanced flexibility and good mechanical properties [1-7]. Moreover, due to the negative impact of global warming and the increasing fuel consumption, renewable and clean energy supply devices drew more and more interest [8, 9]. In this context, supercapacitors, as energy storage devices, have been widely investigated, owing to their advantages like enhanced power density, short charge/discharge time, and low cost [10-14]. However, many challenges remain to find high performance electrodes for supercapacitors that can achieve high energy density (*E*), a measure that is directly connected to the capacitance (*C*) and the operation potential window (*V*) [15]. For battery-like electrodes, the capacity (C or mAh) is typically used to describe the charge storage amount based on a Faradaic reaction [16]. Hence, it is urgent to search for battery-like materials with both high specific/areal capacity and large operation potential window.

Layered double hydroxides (LDHs), $M^{2+}_{1-x}M^{3+}_{x}(OH)_2(A^{n-})_{x/n}\cdot mH_2O$, where [$M^{2+}$ is a bivalent metal cation (Ni^{2+}, Co^{2+}, Cu^{2+}, Mg^{2+}, Mn^{2+}), M^{3+} is a trivalent metal cation (Fe^{3+}, Al^{3+}, V^{3+}, Cr^{3+}), A^{n-} is an interlayer anion (CO_3^{2-}, NO_3^{-}, OH^{-}), and x = M^{3+}/(M^{2+} + M^{3+}) is the surface charge] have been widely applied in supercapacitors, owing to their battery-type characteristics, high redox activity, tunable composition and large active surface area [17-19]. Wu *et al*. designed (N-CNTs)/Co_xNi_{1-x}-layered double hydroxide (Co_xNi_{1-x}-LDHs) nanosheets on Ni foam with a remarkable capacity of 1.62 F cm^{-2} (~810 mC cm^{-2}) at 1 mA cm^{-2} [20]. Lu *et al.* deposited low-crystalline NiAl LDH nanoparticles onto Ni-coated cotton textile, achieving a high capacity of 935.2 mF cm^{-2} (~561.1 mC cm^{-2}) at 5 mV s^{-1} [21]. Guo *et al*. obtained NiMn LDH@Ni foam with an areal capacity of 0.67 F cm^{-2} (~301 mC cm^{-2}) at 3 mA cm^{-2} [22]. Liu *et al*. synthesized a hierarchical CoAl-OH LDH electrode with largely improved capacity of 1031 F g^{-1} (~258 mC cm^{-2}) at 0.5 mA cm^{-2} [23]. Luo *et al*. elaborated $NiCo_2O_4$ core/NiFe LDHs shell ($NiCo_2O_4$@NiFe LDHs) nanowire arrays (NWAs) on carbon cloth (CC) architecture, which reached a high specific capacity of 1.9 F cm^{-2} (~760 mC cm^{-2}) at 1 mA cm^{-2} [24]. Even though high capacity values have been achieved, LDHs-based

electrodes possess a relatively small operating potential window range, usually from 0 to 0.6 V [25-27]. Therefore, the fabrication of hybrid supercapacitors with battery-type materials as positive electrodes and carbon-based materials with large operating potential windows as negative electrodes represents an interesting approach for improving the overall energy density [28-32].

In this work, to explore the influence of Fe, Cr and Al elements on the electrochemical performance of Ni-based LDHs electrodes, NiFe LDHs, NiCr LDHs and NiAl LDHs were prepared on nickel foam (NF) as the supporting collector by hydrothermal method, which is a facile way to synthesize composite materials [33, 34]. Using a similar approach, NiFe LDHs@CS/NF, NiCr LDHs@CS/NF and NiAl LDHs@CS/NF were synthesized on carbon spheres/nickel foam (CS/NF). Among all the prepared binder-free electrodes, NiAl LDHs@CS/NF displayed the largest areal capacity of ~1042.2 mC at 1 mA cm^{-2} and was chosen as a positive electrode to assemble a hybrid supercapacitor. Nitrogen-doped reduced graphene oxide (N-rGO) was further synthesized to act as a negative electrode in the hybrid supercapacitor. Consequently, a flexible NiAl LDHs@CS/NF//N-rGO/NF hybrid supercapacitor device was successfully assembled. The device exhibited favorable flexibility, good mechanical properties and stability (an areal capacity of ~75% and ~67% of the original value was retained after 5,000 and 10,000 cycles, respectively). The hybrid supercapacitor device achieved an energy density of 43 μWh cm^{-2} at a power density of 0.805 mW cm^{-2}, necessary to operate a home-made windmill device continuously for 32 s. Moreover, two as-obtained NiAl LDHs@CS/NF//N-rGO/NF hybrid supercapacitor devices in series were used to light a green LED, a red LED and a yellow LED in parallel simultaneously, lasting for 37 s, 542 s and 199 s, respectively, indicating the potential application of the developed electrodes for flexible energy storage devices.

2. Experimental section

2.1 Synthesis of nitrogen-doped reduced graphene oxide (N-rGO)

N-rGO was prepared through graphene oxide (GO) hydrothermal reduction in presence of hydrazine monohydrate ($NH_2NH_2{\cdot}H_2O$). Typically, 100 mg of GO were dispersed in 50 mL of

Milli-Q water and sonicated for 2 h to form a GO suspension (2 mg mL^{-1}), followed by the addition of 0.5 M hydrazine monohydrate. The resulting mixture was poured into a 100 mL Teflon-lined autoclave and heated at 160 ^{o}C for 3 h. The solution was cooled to room temperature, and the resulting N-rGO was aged in Milli-Q water for 72 h by changing the water every 24 h. Finally, the product was collected by the freezing-dry method for 72 h.

2.2 Preparation of NiCr LDHs/NF, NiFe LDHs/NF and NiAl LDHs/NF

Typically, a homogeneous solution of $Ni(NO_3)_2{\cdot}6H_2O$ (87 mg), $Cr(NO_3)_3{\cdot}9H_2O$ (120 mg), and $CO(NH_2)_2$ (180 mg) in MQ water (35 mL) was prepared through magnetic stirring. NF was dipped into the solution; the mixture was transferred into an autoclave (50 mL) and heated for 12 h at 120 ^{o}C. The resulting NiCr LDHs/NF was rinsed copiously with water, ethanol, and dried in an oven for 24 h at 60 ^{o}C.

$Al(NO_3)_3{\cdot}9H_2O$ (113 mg) and $Fe(NO_3)_3{\cdot}9H_2O$ (121 mg) were used to replace $Cr(NO_3)_3{\cdot}9H_2O$ (120 mg) for the synthesis of NiAl LDHs/NF and NiFe LDHs/NF, respectively.

2.3 Preparation of NiCr LDHs@CS/NF, NiFe LDHs@CS/NF and NiAl LDHs@CS/NF

Typically, a mixture of $Ni(NO_3)_2{\cdot}4H_2O$ (87 mg), $Cr(NO_3)_3{\cdot}9H_2O$ (120 mg) and $CO(NH_2)_2$ (180 mg) in 30 mL MQ water was stirred till formation of a homogeneous solution. The CS/NF was dipped in the above solution, transferred into an autoclave (50 mL), and heated for 12 h at 120 ^{o}C. The resulting NiCr LDHs@CS/NF was rinsed copiously with water, ethanol, and dried for 24 h at 60 ^{o}C.

$Al(NO_3)_3{\cdot}9H_2O$ (113 mg) and $Fe(NO_3)_3{\cdot}9H_2O$ (121 mg) were used to replace $Cr(NO_3)_3{\cdot}9H_2O$ (120 mg) for the synthesis of NiAl LDHs@CS/NF and NiFe LDHs@CS/NF, respectively.

3. Results and discussion

The overall capacity of a hybrid supercapacitor is related to the capacity of the positive and negative electrodes, according to equation (1):

$$\frac{1}{C_T} = \frac{1}{C_p} + \frac{1}{C_n} \quad (1)$$

.

Where C_T is the total capacity of the hybrid supercapacitor, C_p is the capacity of the positive electrode and C_n is the capacity of the negative electrode.

Herein, N-doped reduced graphene oxide coated nickel foam (N-rGO/NF) was first synthesized through hydrothermal reduction of GO in presence of hydrazine monohydrate reducing and doping agent, and applied as a negative electrode with the aim to widen the potential window of a hybrid supercapacitor. The morphology of N-rGO was assessed by scanning electron microscopy (SEM), **Figure 1a**. A porous skeleton consisting of overlapped N-rGO nanosheets could be observed; this morphology is favorable for electrolyte diffusion. **Figure 1b** depicts the Raman spectrum of N-rGO and shows typical D and G bands respectively at 1357 and 1586 cm^{-1} [35].

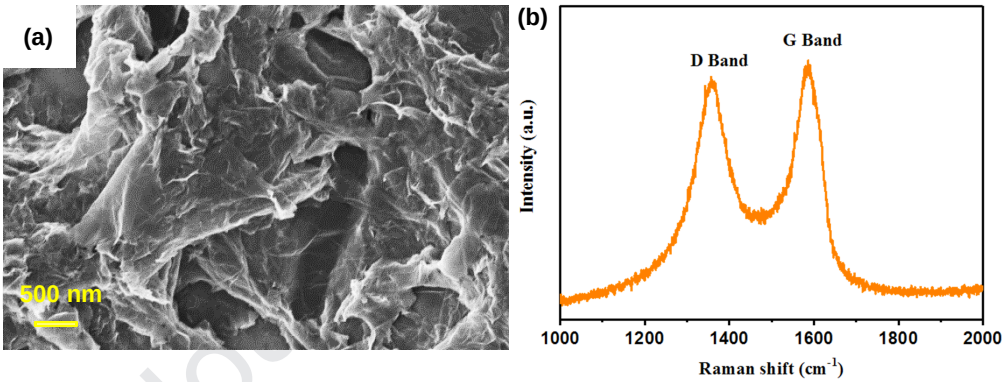

Figure 1: (a) SEM image, and (b) Raman spectrum of N-rGO.

XPS analysis was used to determine the elemental composition of N-rGO. The existence of N element with atomic content of ~3.2 at% proves the successful nitrogen doping of rGO (**Figure 2a**). The spectrum comprises also contributions due to O and C elements with 6 at% and 90.8 at%, respectively.

Figure 2b displays the core level spectrum of the C_{1s}, which can be curve-fitted with four obvious peaks at 284.8, 285.3, 286.9 and 288.9 eV related respectively to the C-C, C-N, C-O, C=O groups. **Figure 2c** reveals the presence of several components at 399.3, 400.6, 402.5 and 407.3 eV in the core level spectrum of the N_{1s} assigned respectively to pyridinic-N, pyrrolic-N, graphitic-N, and oxidized N peaks; the presence of pyridinic-N and pyrrolic-N could potentially enhance electrolyte diffusion and charge transfer in the carbon matrix [36].

The core level spectrum of the O_{1s} comprises several components ascribed to O=C-OH (531.4 eV), C-OH (533.3 eV) and chemisorbed oxygen (535.5 eV), respectively (**Figure 2d**) [37].

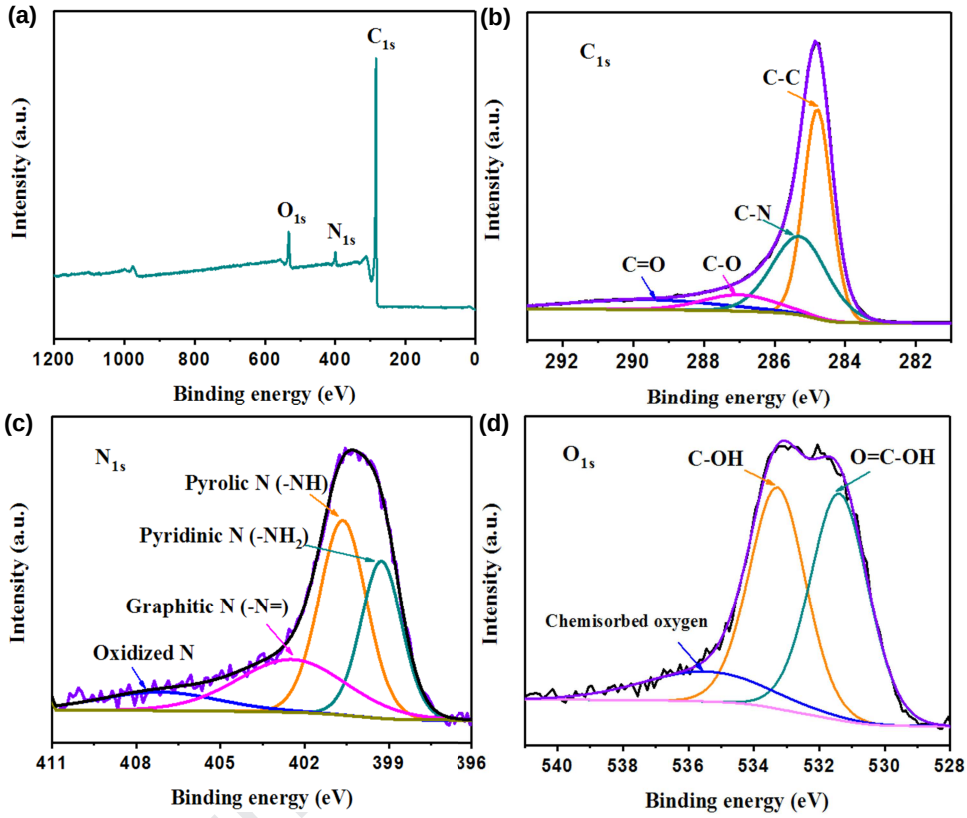

Figure 2: XPS analysis of N-rGO: (a) Survey spectrum and core level spectra of the (b) C_{1s}, (c) N_{1s} and (d) O_{1s}.

As previously stated, the N-rGO was meant to be applied as a negative electrode of a hybrid supercapacitor, so its electrochemical performance was further investigated in a classical 3-electrode cell containing using 2 M KOH electrolyte. **Figure 3a** depicts the galvanostatic charge-discharge (GCD) plots from -1 to +0.4 V of N-rGO/NF electrode at various current densities (1 to 5 mA cm^{-2}), and the corresponding areal capacity values were calculated according to equation (S2). Areal capacity values of 249.1, 185.3, 163.1, 148.3 and 136.2 mC cm^{-2} were determined respectively at 1, 2, 3, 4 and 5 mA cm^{-2} (**Figure 3b**). Furthermore, to get more information on the electrochemical processes at different time constants, impedance spectroscopy (EIS) analysis was performed. The Nyquist plots (**Figure 3c**) reveal the typical depressed semicircle (high-to-medium frequency region) and a straight

line (low-frequency region) arising from ion diffusion in the electrode material. The equivalent circuit is presented in the inset (R_s is the internal resistance, R_{ct} is the charge-transfer resistance, Q is the pseudocapacitance, W_o is the ion transport resistance, C_l is the limit capacitance, and R_l is the limit resistance). The R_s and R_{ct} values were determined to be respectively ~0.78 and ~29.78 ohm cm^{-2}, indicating a good conductivity of N-rGO/NF. All the measurements suggest that N-rGO could be a potential negative electrode material.

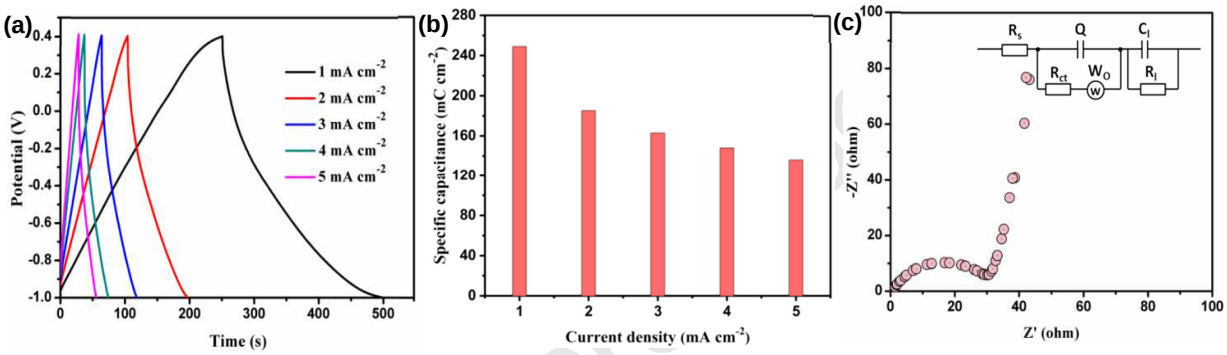

Figure 3: The electrochemical behavior of N-rGO in 2 M KOH solution. (a) GCD plots at various current densities. (b) Areal capacity values at various current densities. (c) EIS acquired at open circuit potential in the frequency range of 0.01 Hz to 100 kHz.

At the same time, layered double hydroxides (LDHs) in this work were chosen as the candidate for the positive electrode of the hybrid supercapacitor. To assess the influence of different trivalent metal elements on the LDHs electrochemical performance, Fe, Cr and Al ions were investigated herein to prepare NiFe LDHs, NiCr LDHs and NiAl LDHs. Moreover, nickel foam (NF) was selected as the current collector, owing to its porosity, 3D framework and excellent electrical conductivity. Nickel foam coated with carbon spheres (NF/CS) was also investigated as a current collector. Consequently, $Ni(OH)_2$/NF, $Ni(OH)_2$@CS/NF, NiFe LDHs/NF, NiFe LDHs@CS/NF, NiCr LDHs/NF, NiCr LDHs@CS/NF, NiAl LDHs/NF and NiAl LDHs@CS/NF were prepared and their electrochemical properties were evaluated. Even with the assistance of carbon spheres (CS), $Ni(OH)_2$@CS/NF displayed poor electrochemical performance (**Figure S1**) with an areal capacity of 74.2 mC cm^{-2} at 1 mA cm^{-2}, which is slightly higher than that of $Ni(OH)_2$/NF (70.6 mC cm^{-2} at 1 mA cm^{-2}). Therefore, these electrodes were not investigated further in detail.

The crystallinity of NiFe LDHs/NF, NiFe LDHs@CS/NF, NiCr LDHs/NF, NiCr LDHs@CS/NF, NiAl LDHs/NF and NiAl LDHs@CS/NF was examined by X-ray diffraction (XRD). As seen in **Figure 4** and **Figure S2**, under the same growth conditions, NiAl LDHs showed obviously better crystallinity than NiFe LDHs and NiCr LDHs. The XRD pattern of NiAl LDHs presents typical (003), (006), (012), (015), (118), (110), (113) and (116) planes for LDHs, appearing at 11.7^o, 23.6^o, 35.1^o, 39.7^o, 47.3^o, 61.2^o, 62.6^o and 66.5^o, respectively (JCPDS No. 15-0087) [38]. Moreover, there are four small peaks of $Ni(OH)_2$ located at 19.3^o, 33.1^o, 38.5^o and 59.4^o ascribed to the (001), (110), (101) and (110) planes, respectively (JCPDS No. 14-0117). Due to the existence of the NF skeleton, the peaks of LDHs exhibit relatively weak intensity so that the magnified XRD pattern in the range of 10–44° was provided in **Figure 4b** for more details. However, for NiFe LDHs@CS/NF and NiCr LDHs@CS/NF samples, no obvious peaks of LDHs were observed owing to the poor crystallinity (**Figure S2**).

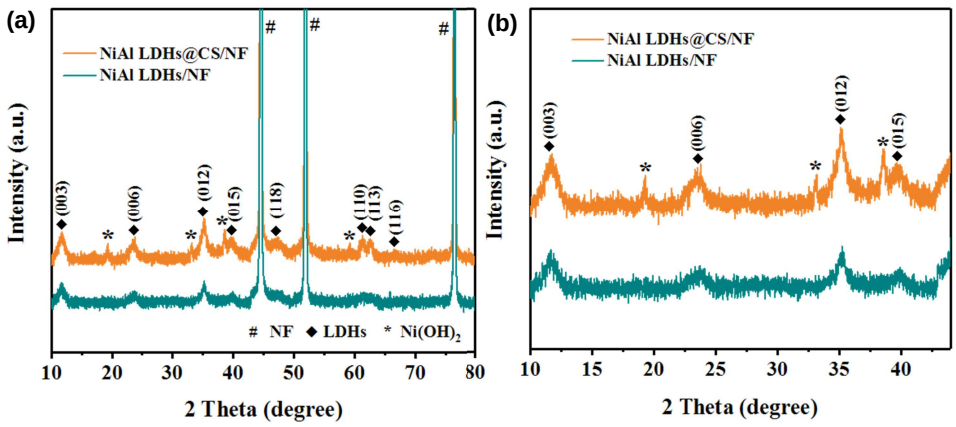

Figure 4: (a) XRD patterns of NiAl LDHs/NF and NiAl LDHs@CS/NF, (b) magnified pattern in the 10–44° range.

Furthermore, the microstructure of the LDH samples was investigated by scanning electron microscopy (**Figure S3, Figure 5**), and showed totally different shapes for the different trivalent elements. **Figure S3a, b** and **Figure 5a, b** display the SEM images of NiFe LDHs/NF and NiFe LDHs@CS/NF, respectively. Interestingly, NiFe LDHs/NF consisted of wool-like nanowires intertwined with each other (**Figure S3a, b**), whereas NiFe

LDHs@CS/NF was composed of abundant nanosheets evenly attached to the surface of the carbon spheres (**Figure 5a, b**). From **Figure S4**, we can see that a carbon spheres (CS, ~400 nm in diameter) layer with a smooth surface was formed on the NF, suggesting the good polymerization/carbonization of glucose during the hydrothermal process [39, 40]. After the growth of NiFe LDHs, all the CSs became pompoms. Notably, the big difference of the morphology between NiFe LDHs/NF and NiFe LDHs@CS/NF might be ascribed to the existence of CS, which leads to differences in crystal growth direction and rate. A thin layer of NiCr LDHs nanosheets was spread on the NF and CS/NF, forming NiCr LDH/NF (**Figure S3c, d**) and NiCr LDHs@CS/NF (**Figure 5c, d**), respectively. However, there is no apparent difference between NiAl LDHs/NF (**Figure S3e, f**) and NiAl LDHs@CS/NF (**Figure 5e, f**), where a dense intertwined nanosheets layer was coated on NF and CS/NF, respectively. Apparently, NiAl LDHs nanosheets grew larger than NiFe LDHs on CS/NF, in which the CSs on NF were completely covered by the NiAl LDHs nanosheets in NiAl LDHs@CS/NF, signifying that NiAl LDHs had faster growth rate under the same conditions, consistent with the XRD results.

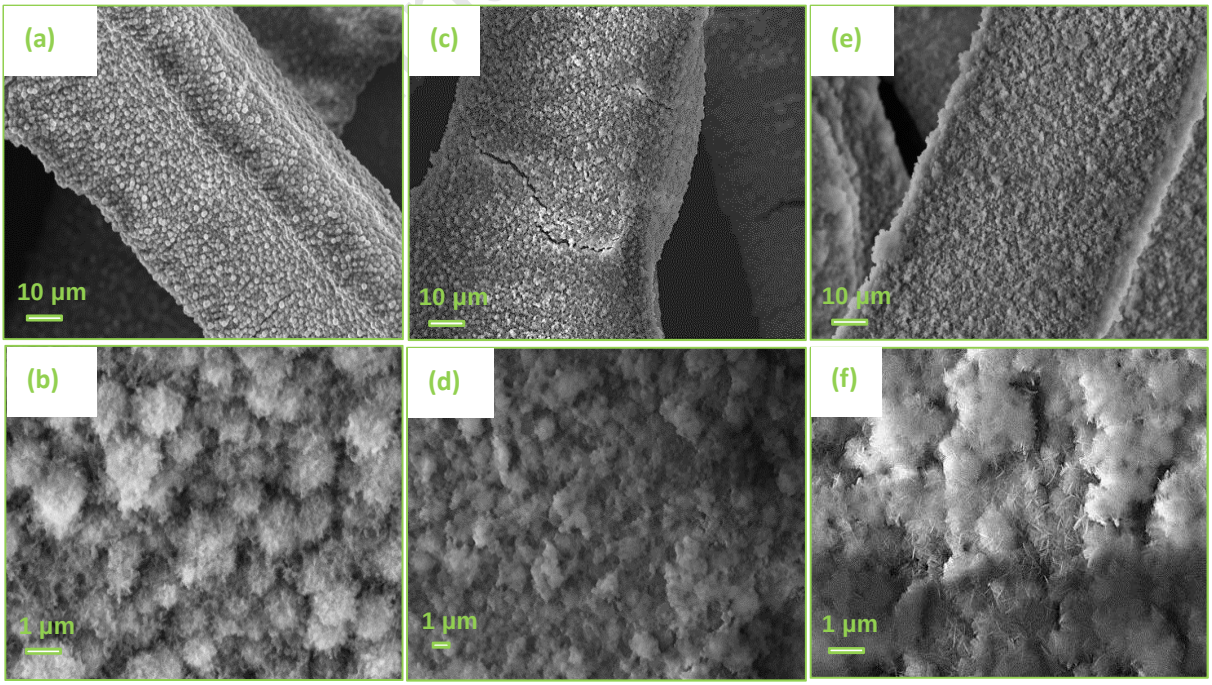

Figure 5: SEM images of (a, b) NiFe LDHs@CS/NF, (c, d) NiCr LDHs@CS /NF and (e, f) NiAl LDHs@CS/NF.

To further assess the chemical composition of the sample, XPS analysis was carried out on NiAl LDHs/NF, NiFe LDHs@CS/NF, NiCr LDHs@CS/NF and NiAl LDHs@CS/NF. From the XPS survey spectra in **Figure S5a** and **Figure 6a-c**, we can see that all the spectra consist of C_{1s}, O_{1s} and Ni_{2p} elements, and the difference is the incorporated trivalent metal cation. For NiFe LDHs@CS/NF, there is also Fe_{2p} element in the spectrum (8.4 at%), **Figure 6a**. **Figure 6a1** displays the core level spectrum of Ni_{2p} (13.7 at%) in NiFe LDHs@CS/NF, where two peaks at 855.7 and 873.4 eV ascribed respectively to $Ni_{2p3/2}$ and $Ni_{2p1/2}$ along with two satellite peaks at 861.1 and 879.6 eV were observed, suggesting that Ni is in +2 oxidation state [41]. The core level spectrum of Fe_{2p} is depicted in **Figure 6a2**, showing two main peaks at 711.4 and 725.1 eV which correspond respectively to $Fe_{2p3/2}$ and $Fe_{2p1/2}$, and two satellite peaks at 716.5 and 732.9 eV, indicating the Fe^{3+} oxidation state in NiFe LDH nanosheets [42]. The wide scan XPS spectrum of NiCr LDHs@CS/NF consists of Ni_{2p} (11.6 at%) and Cr_{2p} (5.9 at%) elements. The high-resolution spectrum of Ni_{2p} in **Figure 6b1** also comprised two peaks located at 856.1 and 873.7 eV due respectively to $Ni_{2p3/2}$ and $Ni_{2p1/2}$, and two satellite peaks at 861.5 and 879.8 eV, proving the existence of Ni^{2+} as well. At the same time, the Cr_{2p} core level spectrum can be deconvoluted with two components at 587.3 and 577.7 eV assigned respectively to $Cr_{2p1/2}$ and $Cr_{2p3/2}$, indicating that Cr is trivalent (**Figure 6b2**) [43].

For NiAl LDHs@CS/NF, the XPS survey spectrum consists of C_{1s}, O_{1s}, Ni_{2p} (8.2 at%) and Al_{2p} (35.3 at%) elements, **Figure 6c**. **Figure S5b** and **Figure 6c1** present the high-resolution ~~spectrum~~ spectra of Ni_{2p} in NiAl LDHs/NF and NiAl LDHs@CS/NF, respectively. Two main peaks at 855.9 and 873.5 eV in NiAl LDHs/NF and 855.7 and 873.4 eV in NiAl LDHs@CS/NF corresponding to $Ni_{2p3/2}$ and $Ni_{2p1/2}$, respectively, and two satellite peaks (861.9 and 880 eV, 861.5 and 879.5 eV) were observed. The high-resolution spectra of the Al_{2p} in NiAl LDHs/NF (**Figure S5c**) and NiAl LDHs@CS/NF (**Figure 6c2**) comprise two peaks ascribed to Al_{2p} at ~73.6 eV along with Ni_{3p} peak at ~68.4 eV [44]. The strong interaction between LDHs and CS caused a small shift of the binding energy of Al_{2p} and Ni_{2p}. **Figure S5d** depicts the core level spectrum of the C_{1s} (14.5 at%) of NiAl LDHs/NF. It can be curve-fitted with three components due to C-C (~284.5 eV), C-O (~285.9 eV) and O-C=O (~288.8 eV) [45].

The C_{1s} core level spectra of NiFe LDHs@CS/NF (27.4 at%), NiCr LDHs@CS/NF (22.4 at%) and NiAl LDHs@CS/NF (16.4 at%) are deconvoluted with four bands ascribed to C=C, C-C, C-O, and O-C=O. The presence of C=C supports the existence of CS in the nanocomposites (**Figure S6a**,**b**,**c**, **Table S1**) [45, 46]. **Figure S5e** and **Figure S6d-f** exhibit the O_{1s} high-resolution spectra of NiAl LDHs/NF, NiFe LDHs@CS/NF, NiCr LDHs@CS/NF and NiAl LDHs@CS/NF, respectively. All of them comprise two peaks ascribed to M-O-M binding (~531.2 eV) and M-OH binding (~531.9 eV) [47]. All the results indicate the successful formation of LDHs.

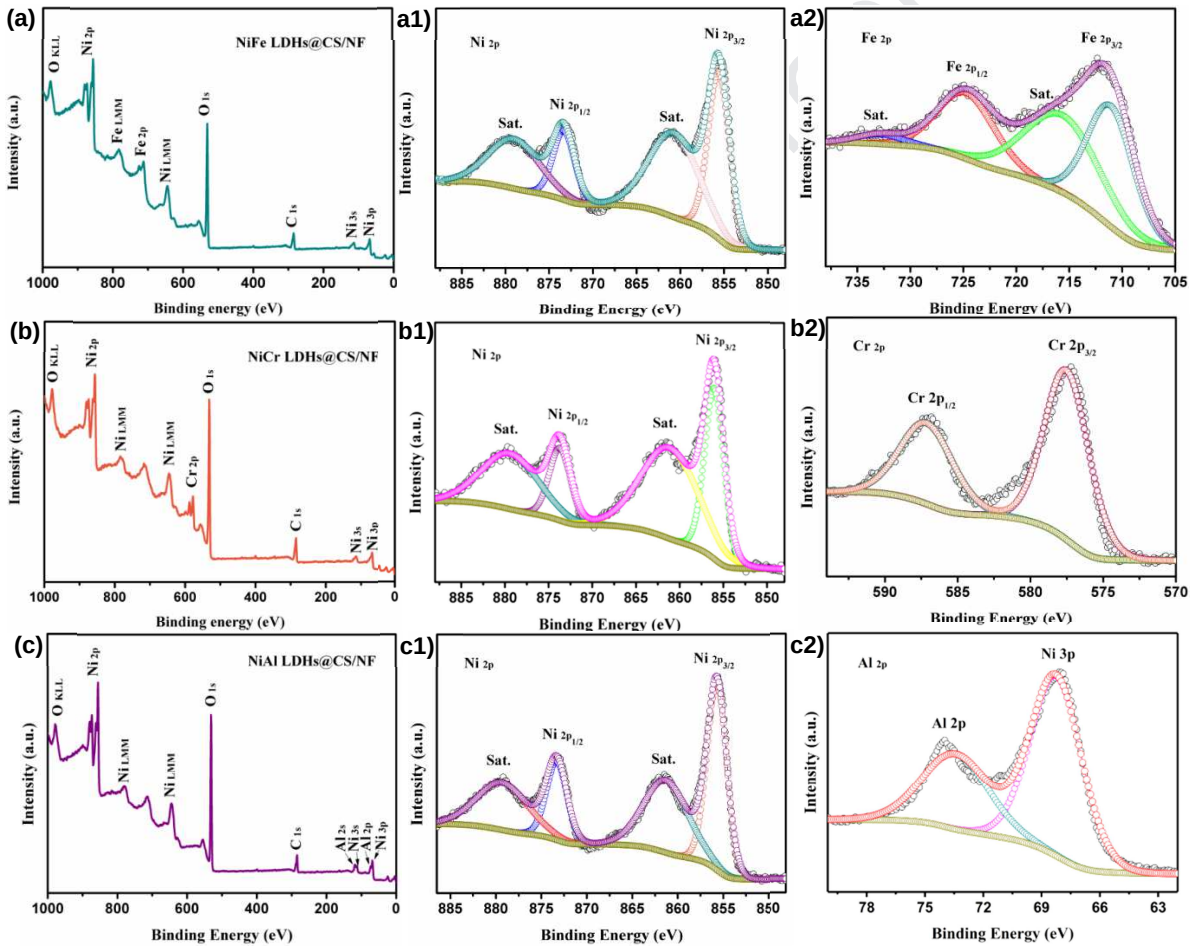

Figure 6: XPS analysis: (a) Survey and core level spectra of (a1) Ni_{2p} and (a2) Fe_{2p} of NiFe LDHs@CS/NF. (b) Survey and core level spectra of (b1) Ni_{2p} and (b2) Cr_{2p} of NiCr LDHs@CS/NF. (c) Survey and core level spectra of (c1) Ni_{2p} and (c2) Al_{2p} of NiAl LDHs@CS/NF.

The electrochemical behavior of all samples was evaluated in a classical 3-electrode cell

in KOH (2 M) aqueous solution (**Figure 7**). From **Figure 7a**, we can see obvious redox active peaks in all the CV plots in the 0 - 0.7 V potential range, corresponding to the following redox process (**Eq. 2**):

$$Ni(OH)_2 + OH^- \leftrightharpoons NiOOH + H_2O + e^- \quad (2)$$

In comparison with the CV plots of $Ni(OH)_2$/NF and $Ni(OH)_2$@CS/NF (**Figure S1a**), the redox peaks separation became more important after LDH formation, which could be due to the synergistic effects of Ni with Fe, Cr, and Al elements.

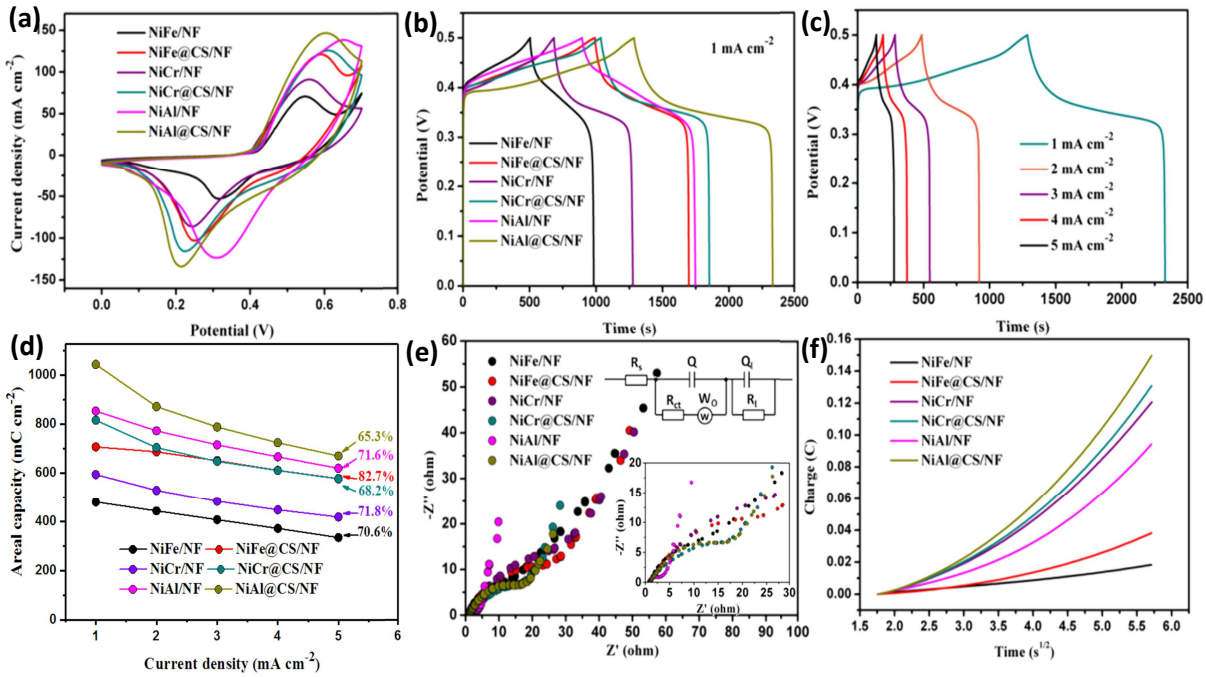

Figure 7: The electrochemical characteristics of the electrodes measured in a classical 3-electrode configuration cell containing 2 M KOH solution. (a) CV plots measured at 50 mV s^{-1}. (b) GCD plots acquired at 1 mA cm^{-2}. (c) GCD profiles of NiAl LDHs@CS/NF at various current densities. (d) Areal capacity at various current densities. (e) EIS recorded at open circuit potential in the 0.01 Hz - 100 kHz frequency range. (f) Q-$t^{1/2}$ plot in 0.1 mM $K_3[Fe(CN)_6]$/0.1 M KCl aqueous solution.

Among all the samples, NiAl LDHs@CS/NF possessed the longest discharge time (**Figure 7b**), signifying the largest areal capacity. According to equation (2), the areal capacity values of NiAl LDHs@CS/NF were determined as 1042.2, 870.2, 787.3, 722.9 and 669 mC cm^{-2} at

respectively 1, 2, 3, 4 and 5 mA cm^{-2}, indicating good rate performance. About 65-80% of areal capacity was maintained even at 5 mA cm^{-2} (**Figure 7c** and **d**). The areal capacity values of all composites are summarized in **Table 1** and compared to other related works from the literature (**Table S2**). From **Table 1** one could observe that the NiAl LDHs/NF exhibited the best performance with areal capacity values of 851.9, 771.4, 714.6, 665.3 and 618.6 mC cm^{-2} at respectively 1, 2, 3, 4 and 5 mA cm^{-2}. Notably, with the incorporation of carbon spheres, the areal capacity of NiFe LDHs@CS/NF, NiCr LDHs@CS/NF and NiAl LDHs@CS/NF were improved by 48%, 37% and 22% compared to NiFe LDHs/NF, NiCr LDHs/NF and NiAl LDHs/NF, respectively. These values outperform those achieved by many LDH-based electrode materials for supercapacitors reported in the literature data (**Table S2**). All the samples presented excellent coulombic efficiencies (see **Table S3**).

Table 1. The areal capacity (mC cm^{-2}) of as-obtained LDH composites.

Current density (mA cm^{-2}) / **Composites**	**1**	**2**	**3**	**4**	**5**
NiFe LDHs /NF	478.6	442.3	406.4	370.6	333.6
NiFe LDHs@CS/NF	705.8	685.7	649.8	610.1	576.6
NiCr LDHs/NF	592.6	527.3	482	446.4	417
NiCr LDHs@CS/NF	814.9	703	646.9	609.6	575.4
NiAl LDHs/NF	851.9	771.4	714.6	665.3	618.6
NiAl LDHs@CS/NF	1042.2	870.2	787.3	722.9	669

To further analyze the ion diffusion (low-frequency region) and charge transfer resistance (high-to-medium frequency region) of the samples, EIS was measured as illustrated in **Figure 7e**. R_s (the intersection of the plot with the X coordinate axis) and R_{ct} (the semicircle) of all the electrodes were obtained from the Nyquist plots and their corresponding values are summarized in **Table S4**. R_s values of 1.28, 1.30, 0.11, 0.94, 0.72 and 1.44 ohm cm^{-2} were determined for NiFe LDHs/NF, NiFe LDHs@CS/NF, NiCr LDHs /NF, NiCr LDHs@CS/NF, NiAl LDHs/NF and NiAl LDHs@CS/NF, respectively, and the corresponding R_{ct} were 10.42,

20.78, 38.78, 14.18, 2.44 and 22.40 ohm cm^{-2}. Compared to NiFe LDHs@CS/NF and NiCr LDHs@CS/NF, NiAl LDHs@CS/NF possessed the smallest R_s but larger R_{ct}, even though it exhibited the largest areal capacity (**Figure 7b** and **d**). This might mainly be ascribed to the larger electrochemical effective surface area.

Consequently, the real electrochemical effective surface area (A) of all electrodes was determined by chronocoulometry experiments using 0.1 mM $K_3[Fe(CN)_6]$ as a probe molecule in 0.1 M KCl (**Figure 7f**), and the charge produced by the redox reaction at the electrodes using the Anson equation:

$$Q(\mathrm{t}) = \frac{2nFAcD^{1/2}t^{1/2}}{\pi^{1/2}} + Q_{dl} + Q_{ads} \quad (3)$$

Where c is the substrate concentration (mol cm^{-3}), n is the number of electron transferred, F is the Faraday constant (9.6485×10^5 C mol^{-1}), A is the effective area of the electrode (cm^2), D stands for the diffusion coefficient (7.6×10^{-6} cm^2 s^{-1}), Q_{ads} is the Faradaic charge, Q_{dl} is the double layer charge, other symbols have their ordinary significance.

From the plot of Q *vs.* $t^{1/2}$ (**Figure 7f**), NiAl LDHs@CS/NF displayed the largest electrochemical effective surface area of 182.8 cm^2, consistent with the above results. Notably, NiAl LDHs/NF holds a smaller electrochemical effective surface area (121.1 cm^2) than that of NiCr LDHs@CS/NF (159.5 cm^2) but larger areal capacity, which may be due to its better conductivity with smaller R_s but larger R_{ct}. As a result, the capacity of the electrode is not only related to conductivity, but also to the real electrochemical effective surface area. Both of them encompass a great effect on the capacitance of the supercapacitors.

A hybrid supercapacitor cell was assembled in which the NiAl LDHs@CS/NF (1 cm×1 cm) was applied as the positive electrode and N-rGO/NF (1.5 cm×1.5 cm) acted as the negative electrode. The CV plots of N-rGO/NF and NiAl LDHs@CS/NF, performed in KOH (2 M) at 100 mV s^{-1} in a classical 2-electrode configuration cell, are presented in **Figure 8a**. Even though N-rGO/NF showed smaller CV area than that of NiAl LDHs@CS/NF, it exhibited a relatively larger operating potential window (-1 to 0.4 V), which is expected to greatly enhance the energy density of the hybrid supercapacitor. In order to find a suitable working voltage window of the hybrid supercapacitor cell, the CV plots were performed at

100 mV s^{-1} in different potential windows of 0-1.1, 0-1.2, 0-1.3, 0-1.4, 0-1.5, 0-1.6, 0-1.7 and 0-1.8 V. As can be seen in **Figure 8b**, the potential window could be extended to 1.8 V, but with the existence of a polarization phenomenon. To protect the electrodes, the potential window was limited to 0-1.6V. Based on the results, the CV plots were acquired at various scan rates between 0 and 1.6 V (**Figure 8c**).

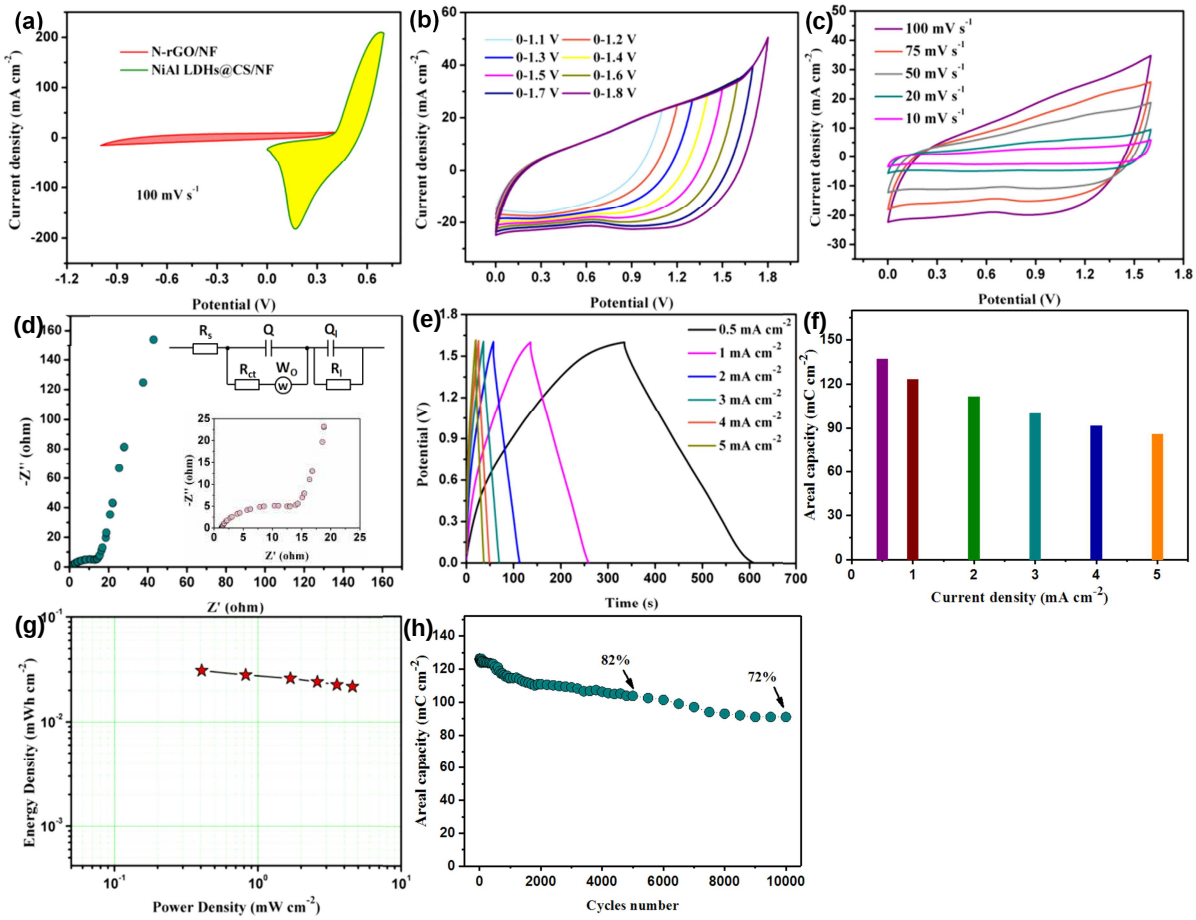

Figure 8: (a) CV curves of N-rGO/NF and NiAl LDHs@CS/NF performed at 100 mV s^{-1} in a 3-electrode cell in KOH (2M) solution. (b) CV plots of the hybrid supercapacitor cell acquired at various potential windows (scan rate=100 mV s^{-1}) in a classical 2-electrode configuration. (c) CV plots of the hybrid supercapacitor cell obtained at various scan rates. (d) EIS analysis of the hybrid supercapacitor cell measured in the 0.01 Hz and 100 kHz frequency range. The inset up-right in (d) is the corresponding equivalent circuit. (e) GCD profiles at various current densities. (f) Areal capacity at various current densities. (g) Ragone plot. (h) Cycling performance of the hybrid supercapacitor cell at 1 mA cm^{-2}.

Furthermore, EIS was recorded in the 100 kHz to 0.01 Hz frequency range; the electrochemical impedance equivalent circuit is displayed in the inset of **Figure 8d**. R_s (the intersection of the plot with the X coordinate axis) and R_{ct} (the semicircle) of all the electrodes, obtained from the Nyquist plots, were 0.38 and 4.30 ohm cm^{-2}, respectively. From the GCD plots recorded at various current densities (**Figure 8e**) and **Eq.2**, the areal capacity of the hybrid supercapacitor cell was calculated as 137.2, 123.1, 111.4, 100.4, 91.7 and 85.8 mC cm^{-2} respectively at 0.5, 1, 2, 3, 4 and 5 mA cm^{-2} (**Figure 8f**). Consequently, according to equations (S5) and (S6), the highest energy density achieved was 31 μWh cm^{-2} at a power density of 0.41 mW cm^{-2} (**Figure 8g**).

Furthermore, the stability of the hybrid supercapacitor cell plays an important role to evaluate its performance. Therefore, the hybrid supercapacitor was submitted to an extended charge-discharge cycling at 1 mA cm^{-2}. After 5,000 cycles, ~82% of the original capacity was retained, which slightly decreased to ~72% after 10,000 cycles (**Figure 8h**).

The SEM images of NiAl LDHs@CS/NF (positive) and N-rGO/NF (negative) electrodes after 5,000 cycles test are displayed in **Figure S7**, where no obvious change of the surface morphology was noticed, suggesting favorable reversibility and stability.

To highlight the potential of the as-fabricated supercapacitor cell for real applications, a home-designed windmill device was assembled successfully (see the schematic diagram in **Figure 9a**); it consists of an engine (1.5-9 V), a windmill and one as-fabricated supercapacitor cell. From **Figure 9a1-4**, we can see that the windmill rotated quickly, and with the consumption of energy, it stopped completely after 21 s.

Furthermore, when two hybrid supercapacitor cells were connected in parallel (insert of **Figure 9b**), the charge-discharge potential window can reach up to 3.2 V with almost the same discharge time. Additionally, the two as-fabricated hybrid supercapacitor cells in series were applied to supply electricity to a red LED (1.8-2 V), a green LED (3-3.6 V) and a yellow LED (1.9-2.4 V) in parallel. The green, yellow and red LEDs were lightened for 37, 195, and 459 s, respectively (**Figure 9b1-b5**). All of these findings demonstrate a promising practical energy storage application of the as-fabricated hybrid supercapacitor cells.

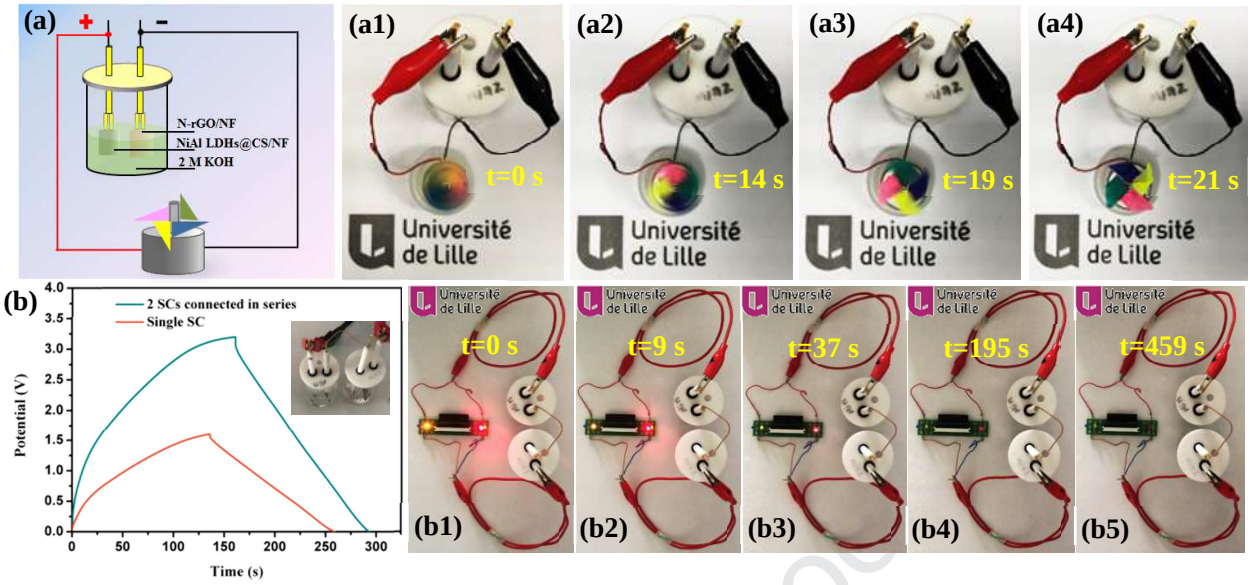

Figure 9. (a) Schematic of the hybrid supercapacitor cell operating a homemade windmill device. (a1 to a4) Photographs of the home-designed windmill device operation. (b) GCD curves of a single supercapacitor and two supercapacitors in series. The inset depicts the photograph of the two supercapacitors in series. (b1 to b5) A red LED, a green LED and a yellow LED in parallel lighten up by two supercapacitor cells in series.

Finally, a flexible hybrid supercapacitor device was assembled in which NiAl LDHs@CS/NF (1 cm×1 cm) was applied as a positive electrode, N-rGO/NF (1.5 cm×1.5 cm) as a negative electrode, and one piece of filter paper immersed into KOH (2 M) aqueous solution as a separator (**Figure 10a**). The electrochemical behavior of the device was assessed in a 2-electrode system, and the CV plots acquired at various potential windows (scan rate = 100 mV s^{-1}) are displayed in **Figure 10b**. The results revealed that the potential window could reach up to 1.8 V even though a polarization phenomenon was obvious when the potential exceeds 1.7 V. In order to reduce the damage to the electrode and ensure stable operation of the device, the operating potential window was chosen as 0-1.6V. **Figure 10c** displays the CV curves of the hybrid supercapacitor obtained at various scan rates (10 - 100 mV s^{-1}) between 0 and 1.6 V. The full device exhibited a capacitive-like characteristic with obvious deviation from ideal capacitive behavior although NiAl LDHs@CS/NF electrode performed as a battery-type electrode [16]. At the same time, as displayed in the Nyquist plot (**Figure 10d**), we can observe that the whole system reveals a smaller internal resistance

(R_s=0.20 ohm cm^{-2}) and charge-transfer resistance (R_{ct}=0.84 ohm cm^{-2}) than that of the hybrid supercapacitor cell. A possible reason might be that the two integrated electrodes shorten the distance of electron transfer and ion diffusion. Consequently, the hybrid supercapacitor device exhibited a longer discharge time than that of the hybrid supercapacitor cell, signifying a larger areal capacity (**Figure 10e** and **f**).

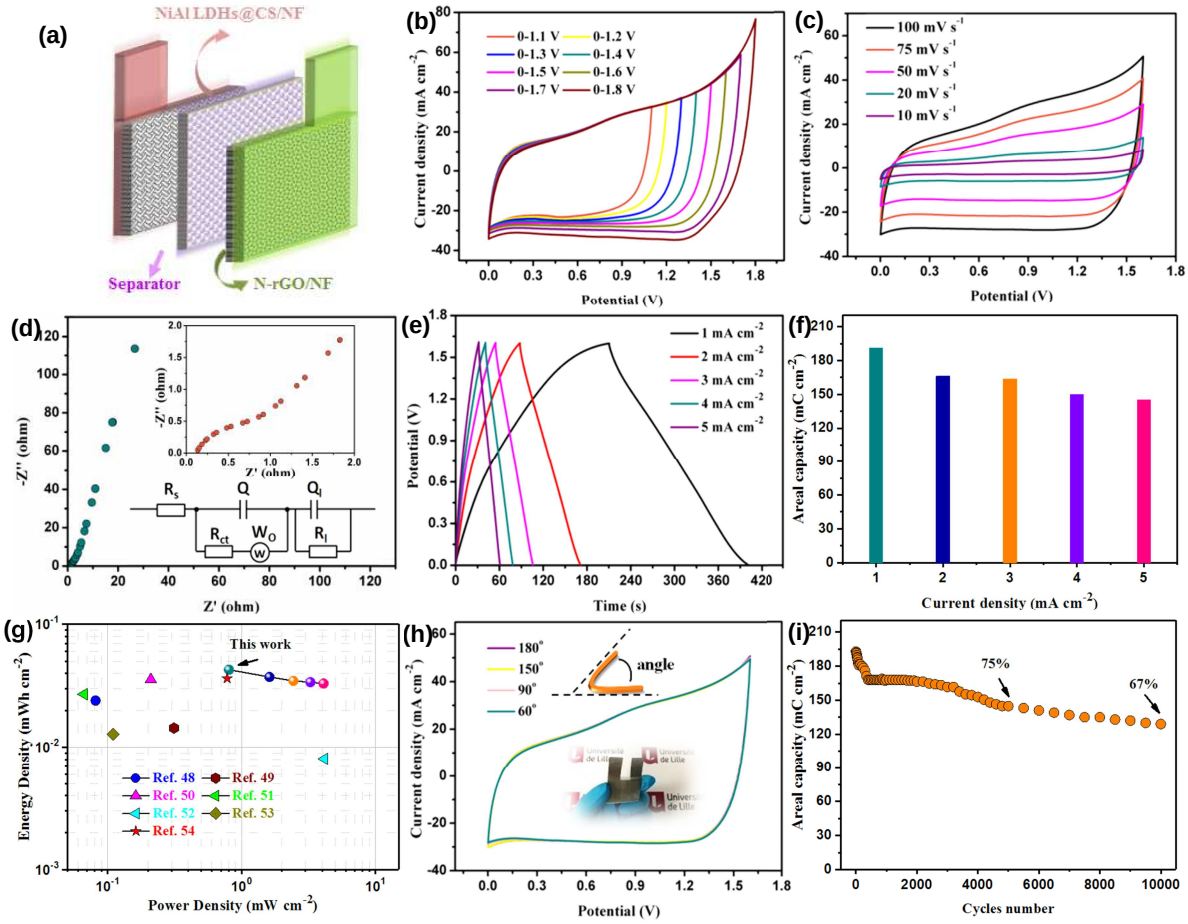

Figure 10: (a) Schematic of the hybrid supercapacitor. CV plots measured at (b) various potential windows at 100 mV s^{-1} and (c) various scan rates between 0 and 1.6 V. (d) EIS curves acquired in the 0.01 Hz and 100 kHz frequency range. The inset up-right in (d) is the equivalent circuit. (e) GCD plots at various current densities. (f) Areal capacity at various current densities. (g) Ragone plot. (h) CV plots acquired at 100 mV s^{-1} at different bending angles. The inset in middle of (h) is the photograph of the hybrid supercapacitor device. (i) Cycling performance at 1 mA cm^{-2}.

According to equation (2), the areal capacity of the hybrid supercapacitor device was

calculated as 191.3, 166.1, 153.7, 149.8 and 145.2 mC cm^{-2} respectively at 1, 2, 3, 4 and 5 mA cm^{-2} (**Figure 10f**). According to equations (5) and (6), the hybrid supercapacitor device attained the largest areal energy density of 43 μWh cm^{-2} at a power density of 0.805 mW cm^{-2} (**Figure 10g**). This value is higher than that achieved by Ni-Co LDH//ketjenblack (14.4 μWh cm^{-2} at 312.5 μW cm^{-2}) [48], Mg-Al LDH//rGO (24.07 μWh cm^{-2} at 81.2 μW cm^{-2}) [49], $Co_{0.85}Se$//AC (35.65 μWh cm^{-2} at 210 μW cm^{-2}) [50] hybrid supercapacitors, HCF fiber (27.1 μWh cm^{-2} at 66.5 μW cm^{-2}) [51], rGO/V_2O_5-rGO asymmetric flexible device (8.1 μWh cm^{-2} at 4.17 mW cm^{-2}) [52], Cu@Ni/porous Ni/$MnCo_2O_4$ symmetric supercapacitor (12.8 μWh cm^{-2} at 110 μW cm^{-2}) [53] and MnO_2/CNT//PI/CNT asymmetric supercapacitor (36.4 μWh cm^{-2} at 0.78 mW cm^{-2}) [54].

Furthermore, to test the flexibility and mechanical properties of the device and meet wearable requirements, the hybrid supercapacitor device in the middle of **Figure 10h** was bent at different angles (150, 90 and 60°); the CV curves, acquired at different angles, are almost overlapping together, indicating excellent flexibility and mechanical properties and providing promising potential for their application in wearable energy devices.

Additionally, the hybrid supercapacitor stability after 10,000 charging–discharging cycles was measured; the areal capacity remained ~75% and ~67% of its original value respectively after 5,000 and 10,000 cycles, suggesting a good reversibility (**Figure 10i**).

Furthermore, to test the practical applicability of the packed hybrid supercapacitor device, it was applied for a windmill device operation (schematic diagram in **Figure 11a**). Upon its connection with the hybrid supercapacitor device, the windmill rotates quickly and continuously for 32 s (**Figure 11b-e**).

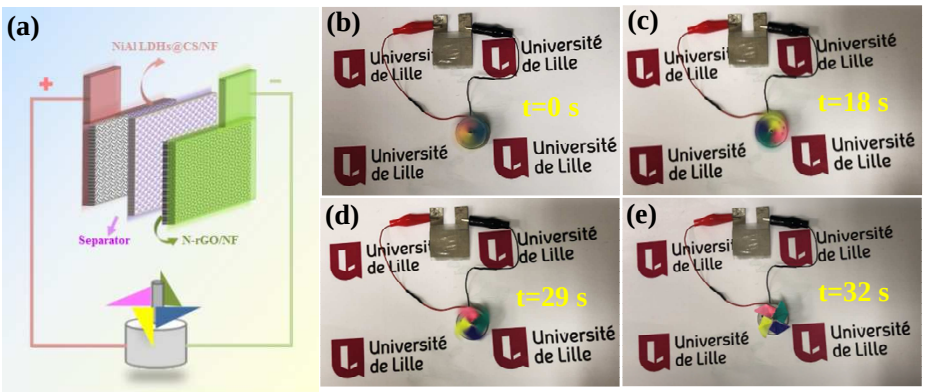

Figure 11. (a) Schematic diagram of the hybrid supercapacitor device for operating a homemade windmill device. (b-e) Photographs of the home-designed windmill device operation.

Finally, as shown in **Figure 12a-b**, when two hybrid supercapacitors were connected in series as the power source, the work potential window can reach 3.2 V to supply power to 3 LEDs in parallel. The device can successfully light up three LEDs at the same time (**Figure 12c-h**). With the consumption of electricity, the light gradually dims and the green light (3-3.6 V) went out after 37 s (**Figure 12e**), followed by the yellow one (1.9-2.4 V) after 199 s (**Figure 12g**). The red LED (1.8-2 V) becomes very dark, but still lights up until 542 s. All the results suggest that the as-assembled hybrid supercapacitor device possesses a promising potential for flexible energy storage applications.

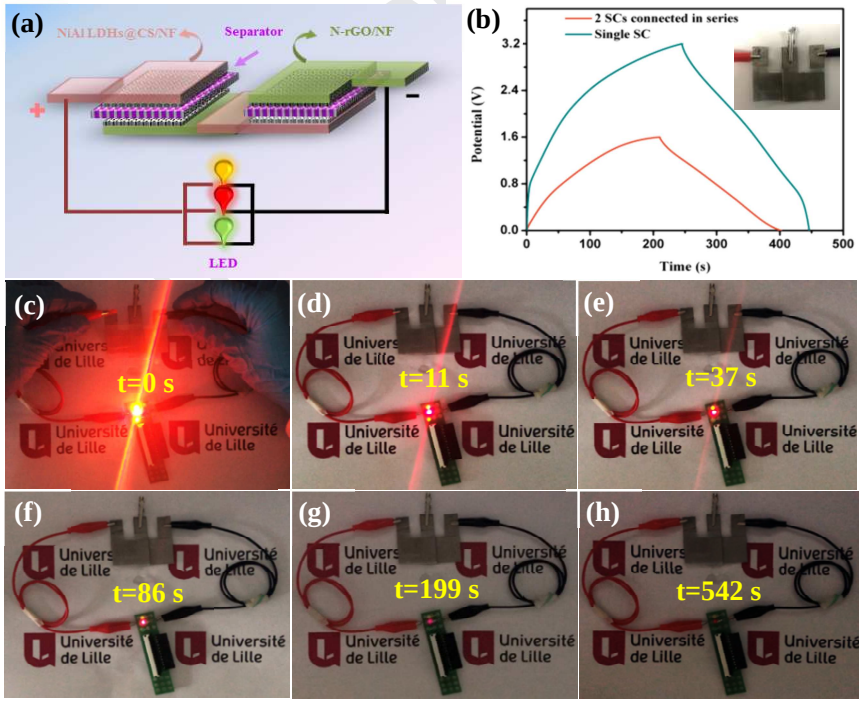

Figure 12. (a) Schematic diagram of the hybrid supercapacitor in series for lighting of LEDs in parallel. (b) GCD plots of a single supercapacitor and two supercapacitors in series. The inset depicts the photograph of the two supercapacitors devices in series. (c to h) A yellow LED, a red LED and a green LED in parallel lighted up by two supercapacitors in series.

4. Conclusion

In summary, NiFe LDHs, NiCr LDHs and NiAl LDHs on nickel foam (NF) were synthesized by a simple hydrothermal process. With the assistance of carbon spheres (CS), NiFe LDHs@CS/NF, NiCr LDHs@CS/NF and NiAl LDHs@CS/NF were further obtained. Among all the samples, NiAl LDHs@CS/NF exhibited the best electrochemical performance as a binder-free electrode and the largest areal capacity of 1042.2 mC cm^{-2} at 1 mA cm^{-2}. Consequently, NiAl LDHs@CS/NF//N-rGO/NF hybrid supercapacitor cell in KOH solution and flexible NiAl LDHs@CS/NF//N-rGO/NF hybrid supercapacitor devices were successfully assembled, and further applied for windmill device operation, lasting for 21 and 32 s, respectively. Moreover, two NiAl LDHs@CS/NF//N-rGO/NF hybrid supercapacitor cells connected in series were able to supply electricity to LEDs in parallel and the red one was lighted up for the longest time of ~459 s. The flexible NiAl LDHs@CS/NF//N-rGO/NF hybrid supercapacitor device displayed favorable flexibility, mechanical properties and stability; two devices in series could light a yellow LED (199 s), a red LED (542 s) and a green LED (37 s) in parallel simultaneously. All the findings suggest that the developed electrodes hold a promising potential for energy storage applications.

References

[1] T. Lv, M. Liu, D. Zhu, L. Gan, T. Chen, Nanocarbon-Based Materials for Flexible All-Solid-State Supercapacitors, Adv. Mater. 30 (2018) e1705489.

[2] C. Shen, Y. Xie, M. Sanghadasa, Y. Tang, L. Lu, L. Lin, Ultrathin Coaxial Fiber Supercapacitors Achieving High Energy and Power Densities, ACS Appl. Mater. Interfaces 9 (2017) 39391-39398.

[3] B. Patil, S. Ahn, S. Yu, H. Song, Y. Jeong, J.H. Kim, H. Ahn, Electrochemical performance of a coaxial fiber-shaped asymmetric supercapacitor based on nanostructured MnO_2/CNT-web paper and Fe_2O_3/carbon fiber electrodes, Carbon 134 (2018) 366-375.

[4] J. Zhao, J. Chen, S. Xu, M. Shao, Q. Zhang, F. Wei, J. Ma, M. Wei, D.G. Evans, X. Duan, Hierarchical NiMn Layered Double Hydroxide/Carbon Nanotubes Architecture with Superb Energy Density for Flexible Supercapacitors, Adv. Funct. Mater. 24 (2014) 2938-2946.

[5] Z. Lv, Y. Luo, Y. Tang, J. Wei, Z. Zhu, X. Zhou, W. Li, Y. Zeng, W. Zhang, Y. Zhang, D. Qi, S. Pan, X.J. Loh, X. Chen, Editable Supercapacitors with Customizable Stretchability Based on Mechanically Strengthened Ultralong MnO_2 Nanowire Composite, Adv. Mater. 30 (2018) 1704531.

[6] J. Huang, Y. Xiao, Z. Peng, Y. Xu, L. Li, L. Tan, K. Yuan, Y. Chen, Co_3O_4 Supraparticle-Based Bubble Nanofiber and Bubble Nanosheet with Remarkable Electrochemical Performance, Adv. Sci. 6 (2019) 1900107.

[7] P. Simon, Y. Gogotsi, Materials for electrochemical capacitors, Nat. Mater. 7 (2008) 845-854.

[8] N. Choudhary, C. Li, H.S. Chung, J. Moore, J. Thomas, Y. Jung, High-Performance One-Body Core/Shell Nanowire Supercapacitor Enabled by Conformal Growth of Capacitive 2D WS_2 Layers, ACS Nano 10 (2016) 10726-10735.

[9] M.J. Deng, J.K. Chang, C.C. Wang, K.W. Chen, C.M. Lin, M.T. Tang, J.M. Chen, K.T. Lu, High-performance electrochemical pseudo-capacitor based on MnO_2 nanowires/Ni foam as electrode with a novel Li-ion quasi-ionic liquid as electrolyte, Energy Environ. Sci. 4 (2011) 3942.

[10] G. Luo, K. Siong Teh, Y. Xia, Y. Luo, Z. Li, S. Wang, L. Zhao, Z. Jiang, A novel three-dimensional spiral CoNi LDHs on Au@ErGO wire for high performance fiber supercapacitor electrodes, Mater. Lett. 236 (2019) 728-731.

[11] J. Zhu, T. Feng, X. Du, J. Wang, J. Hu, L. Wei, High performance asymmetric supercapacitor based on polypyrrole/graphene composite and its derived nitrogen-doped carbon nano-sheets, J. Power Sources 346 (2017) 120-127.

[12] X. Zhang, S. Deng, Y. Zeng, M. Yu, Y. Zhong, X. Xia, Y. Tong, X. Lu, Oxygen Defect Modulated Titanium Niobium Oxide on Graphene Arrays: An Open-Door for High-Performance 1.4 V Symmetric Supercapacitor in Acidic Aqueous Electrolyte, Adv. Funct. Mater. 28 (2018) 1805618.

[13] H. Jia, J. Sun, X. Xie, K. Yin, L. Sun, Cicada slough-derived heteroatom incorporated porous carbon for supercapacitor: Ultra-high gravimetric capacitance, Carbon 143 (2019) 309-317.

[14] X. Mu, D. Wang, F. Du, G. Chen, C. Wang, Y. Wei, Y. Gogotsi, Y. Gao, Y. Dall'Agnese,

Revealing the Pseudo-Intercalation Charge Storage Mechanism of MXenes in Acidic Electrolyte, Adv. Funct. Mater. 29 (2019) 1902953.

[15] J. Zhu, W. Sun, D. Yang, Y. Zhang, H.H. Hoon, H. Zhang, Q. Yan, Multifunctional Architectures Constructing of PANI Nanoneedle Arrays on MoS2 Thin Nanosheets for High-Energy Supercapacitors, Small 11 (2015) 4123-4129.

[16] Y. Shao, M.F. El-Kady, J. Sun, Y. Li, Q. Zhang, M. Zhu, H. Wang, B. Dunn, R.B. Kaner, Design and Mechanisms of Asymmetric Supercapacitors, Chem. Rev. 118 (2018) 9233-9280.

[17] Z. Gao, C. Bumgardner, N. Song, Y. Zhang, J. Li, X. Li, Cotton-textile-enabled flexible self-sustaining power packs via roll-to-roll fabrication, Nat. Commun. 7 (2016) 11586.

[18] X. Wang, J. Zhang, S. Yang, H. Yan, X. Hong, W. Dong, Y. Liu, B. Zhang, Z. Wen, Interlayer space regulating of NiMn layered double hydroxides for supercapacitors by controlling hydrothermal reaction time, Electrochim. Acta 295 (2019) 1-6.

[19] X. Li, D. Du, Y. Zhang, W. Xing, Q. Xue, Z. Yan, Layered double hydroxides toward high-performance supercapacitors, J. Mater. Chem. A 5 (2017) 15460-15485.

[20] J. Wu, W.W. Liu, Y.X. Wu, T.C. Wei, D. Geng, J. Mei, H. Liu, W.M. Lau, L.M. Liu, Three-dimensional hierarchical interwoven nitrogen-doped carbon nanotubes/Co_xNi_{1-x}-layered double hydroxides ultrathin nanosheets for high-performance supercapacitors, Electrochim. Acta 203 (2016) 21-29.

[21] H. Lu, J. Chen, Q. Tian, Wearable high-performance supercapacitors based on Ni-coated cotton textile with low-crystalline Ni-Al layered double hydroxide nanoparticles, J. Colloid Interf. Sci. 513 (2018) 342-348.

[22] X.L. Guo, X.Y. Liu, X.D. Hao, S.J. Zhu, F. Dong, Z.Q. Wen, Y.X. Zhang, Nickel-Manganese Layered Double Hydroxide Nanosheets Supported on Nickel Foam for High-performance Supercapacitor Electrode Materials, Electrochim. Acta 194 (2016) 179-186.

[23] X. Liu, A. Zhou, T. Pan, Y. Dou, M. Shao, J. Han, M. Wei, Ultrahigh-rate-capability of a layered double hydroxide supercapacitor based on a self-generated electrolyte reservoir, J. Mater. Chem. A 4 (2016) 8421-8427.

[24] G. Luo, K.S. Teh, Y. Xia, Z. Li, Y. Luo, L. Zhao, Z. Jiang, Construction of $NiCo_2O_4$ @NiFe LDHs core/shell nanowires array on carbon cloth for flexible, high-performance

pseudocapacitor electrodes, J. Alloys Compd. 767 (2018) 1126-1132.

[25] P.F. Liu, J.J. Zhou, G.C. Li, M.K. Wu, K. Tao, F.Y. Yi, W.N. Zhao, L. Han, A hierarchical NiO/NiMn-layered double hydroxide nanosheet array on Ni foam for high performance supercapacitors, Dalton Trans. 46 (2017) 7388-7391.

[26] M. Padmini, S.K. Kiran, N. Lakshminarasimhan, M. Sathish, P. Elumalai, High-performance Solid-state Hybrid Energy-storage Device Consisting of Reduced Graphene-Oxide Anchored with NiMn-Layered Double Hydroxide, Electrochim. Acta 236 (2017) 359-370.

[27] X. Liu, C. Wang, Y. Dou, A. Zhou, T. Pan, J. Han, M. Wei, A NiAl layered double hydroxide@carbon nanoparticles hybrid electrode for high-performance asymmetric supercapacitors, J. Mater. Chem. A 2 (2014) 1682-1685.

[28] S. Li, P. Cheng, J. Luo, D. Zhou, W. Xu, J. Li, R. Li, D. Yuan, High-Performance Flexible Asymmetric Supercapacitor Based on CoAl-LDH and rGO Electrodes, Nano-Micro Lett 9 (2017) 31.

[29] W. Guo, C. Yu, S. Li, J. Yang, Z. Liu, C. Zhao, H. Huang, M. Zhang, X. Han, Y. Niu, J. Qiu, High-Stacking-Density, Superior-Roughness LDH Bridged with Vertically Aligned Graphene for High-Performance Asymmetric Supercapacitors, Small 13 (2017) 1701288.

[30] X. Wang, X. Li, X. Du, X. Ma, X. Hao, C. Xue, H. Zhu, S. Li, Controllable Synthesis of NiCo LDH Nanosheets for Fabrication of High-Performance Supercapacitor Electrodes, Electroanalysis 29 (2017) 1286-1293.

[31] L. Liu, L. Fang, F. Wu, J. Hu, S. Zhang, H. Luo, B. Hu, M. Zhou, Self-supported core-shell heterostructure MnO_2/NiCo-LDH composite for flexible high-performance supercapacitor, J. Alloys Compd. 824 (2020) 153929.

[32] Q. Qin, D. Ou, C. Ye, L. Chen, B. Lan, J. Yan, Y. Wu, Systematic study on hybrid supercapacitor of Ni-Co layered double hydroxide//activated carbons, Electrochim. Acta 305 (2019) 403-415.

[33] T. Zhou, Z. Zang, J. Wei, J. Zheng, J. Hao, F. Ling, X. Tang, L. Fang, M. Zhou, Efficient charge carrier separation and excellent visible light photoresponse in Cu_2O nanowires, Nano Energy, 50 (2018) 118-125.

[34] H. Wang, P. Zhang, Z. Zang, High performance $CsPbBr_3$ quantum dots photodetectors

by using zinc oxide nanorods arrays as an electron-transport layer, Appl. Phy. Lett. 116 (2020) 162103.

[35] M. Kang, D.H. Lee, Y.M. Kang, H. Jung, Electron beam irradiation dose dependent physico-chemical and electrochemical properties of reduced graphene oxide for supercapacitor, Electrochim. Acta 184 (2015) 427-435.

[36] S.K. Singh, V.M. Dhavale, R. Boukherroub, S. Kurungot, S. Szunerits, N-doped porous reduced graphene oxide as an efficient electrode material for high performance flexible solid-state supercapacitor, Appl. Mater. Today 8 (2017) 141-149.

[37] N.M. Latiff, C.C. Mayorga-Martinez, L. Wang, Z. Sofer, A.C. Fisher, M. Pumera, Microwave irradiated N- and B,Cl-doped graphene: Oxidation method has strong influence on capacitive behavior, Appl. Mater. Today 9 (2017) 204-211.

[38] W. Wang, N. Zhang, Z. Shi, Z. Ye, Q. Gao, M. Zhi, Z. Hong, Preparation of Ni-Al layered double hydroxide hollow microspheres for supercapacitor electrode, Chem. Eng. J. 338 (2018) 55-61.

[39] Y. Zhang, M. Dong, S. Zhu, C. Liu, Z. Wen, MnO_2@colloid carbon spheres nanocomposites with tunable interior architecture for supercapacitors, Mater. Res. Bull. 49 (2014) 448-453.

[40] P.N. Bhagat, K.R. Patil, D.S. Bodas, K.M. Paknikar, Hydrothermal synthesis and characterization of carbon nanospheres: a mechanistic insight, RSC Adv. 5 (2015) 59491-59494.

[41] J. Zhao, L. Cai, H. Li, X. Shi, X. Zheng, Stabilizing Silicon Photocathodes by Solution-Deposited Ni-Fe Layered Double Hydroxide for Efficient Hydrogen Evolution in Alkaline Media, ACS Energy Lett. 2 (2017) 1939-1946.

[42] J. Liu, J. Wang, B. Zhang, Y. Ruan, L. Lv, X. Ji, K. Xu, L. Miao, J. Jiang, Hierarchical $NiCo_2S_4$@NiFe LDH Heterostructures Supported on Nickel Foam for Enhanced Overall-Water-Splitting Activity, ACS Appl. Mater. Interfaces 9 (2017) 15364-15372.

[43] Y. Yang, L. Dang, M.J. Shearer, H. Sheng, W. Li, J. Chen, P. Xiao, Y. Zhang, R.J. Hamers, S. Jin, Highly Active Trimetallic NiFeCr Layered Double Hydroxide Electrocatalysts for Oxygen Evolution Reaction, Adv. Energy Mater. 8 (2018) 1703189.

[44] M. Jarosz, R.P. Socha, P. Jóźwik, G.D. Sulka, Amperometric glucose sensor based on the

$Ni(OH)_2/Al(OH)_4$ - electrode obtained from a thin Ni_3Al foil, Appl. Surf. Sci. 408 (2017) 96-102.

[45] J. Xu, X. Li, X. Li, S. Li, L. Zhao, D. Wang, W. Xing, Z. Yan, Free-standing cotton-derived carbon microfiber@nickel-aluminum layered double hydroxides composite and its excellent capacitive performance, J. Alloys Compd. 787 (2019) 27-35.

[46] X. Wang, J. Liu, W. Xu, One-step hydrothermal preparation of amino-functionalized carbon spheres at low temperature and their enhanced adsorption performance towards Cr(VI) for water purification, Colloids Surf. A Physicochem. Eng. Asp. 415 (2012) 288-294.

[47] L. Wang, X. Huang, S. Jiang, M. Li, K. Zhang, Y. Yan, H. Zhang, J.M. Xue, Increasing Gas Bubble Escape Rate for Water Splitting with Nonwoven Stainless Steel Fabrics, ACS Appl. Mater. Interfaces 9 (2017) 40281-40289.

[48] M. Yang, H. Cheng, Y. Gu, Z. Sun, J. Hu, L. Cao, F. Lv, M. Li, W. Wang, Z. Wang, S. Wu, H. Liu, Z. Lu, Facile electrodeposition of 3D concentration-gradient Ni-Co hydroxide nanostructures on nickel foam as high performance electrodes for asymmetric supercapacitors, Nano Res. 8 (2015) 2744-2754.

[49] G. Hatui, G.C. Nayak, G. Udayabhanu, One Pot Solvothermal Synthesis of Sandwich-like Mg Al Layered Double Hydroxide anchored Reduced Graphene Oxide: An excellent electrode material for Supercapacitor, Electrochim Acta 219 (2016) 214-226.

[50] J. Yang, Y. Yuan, W. Wang, H. Tang, Z. Ye, J. Lu, Interconnected $Co_{0.85}Se$ nanosheets as cathode materials for asymmetric supercapacitors, J. Power Sources 340 (2017) 6-13.

[51] G. Qu, J. Cheng, X. Li, D. Yuan, P. Chen, X. Chen, B. Wang, H. Peng, A Fiber Supercapacitor with High Energy Density Based on Hollow Graphene/Conducting Polymer Fiber Electrode, Adv. Mater. 28 (2016) 3646-3652.

[52] C.Y. Foo, A. Sumboja, D.J.H. Tan, J. Wang, P.S. Lee, Flexible and Highly Scalable V_2O_5-rGO Electrodes in an Organic Electrolyte for Supercapacitor Devices, Adv. Energy Mater. 4 (2014) 1400236.

[53] Y. Ji, J. Xie, J. Wu, Y. Yang, X.Z. Fu, R. Sun, C.P. Wong, Hierarchical nanothorns $MnCo_2O_4$ grown on porous/dense Ni bi-layers coated Cu wire current collectors for high performance flexible solid-state fiber supercapacitors, J. Power Sources 393 (2018) 54-61.

[54] G. Huang, Y. Zhang, L. Wang, P. Sheng, H. Peng, Fiber-based MnO_2/carbon

nanotube/polyimide asymmetric supercapacitor, Carbon 125 (2017) 595-604.

Highlights

- NiAl LDH decorated on carbon spheres supported on Ni foam was prepared
- The electrode material exhibited a high areal capacity of 1042.2 mC cm^{-2} at 1 mA cm^{-2}
- A supercapacitor was assembled and exhibited a high energy density of 43 μWh cm^{-2} at a power density of 0.805 mW cm^{-2}
- The supercapacitor was able to operate a home-designed windmill device for 32 s
- The supercapacitor was used to light up a green, a red and a yellow LED

Declaration of interests

☒ The authors declare that they have no known competing financial interests or personal relationships that could have appeared to influence the work reported in this paper.

☐The authors declare the following financial interests/personal relationships which may be considered as potential competing interests: